



Reagentless impedimetric immunosensor for monitoring of methotrexate in human blood serum using multiwalled carbon nanotube@polypyrrole/polytyramine film electrode

Kayode Omotayo Adeniyi^{a,*}, Blerina Osmanaj^{a,b}, Gopinathan Manavalan^a, Jyri-Pekka Mikkola^{a,c}, Avni Berisha^b, Solomon Tesfalidet^{a,**}

^a Department of Chemistry, Umeå University, Umeå, 90187, Sweden

^b Department of Chemistry, University of Prishtina, 10000, Prishtina, Republic of Kosovo

^c Industrial Chemistry and Reaction Engineering, Johan Gadolin Process Chemistry Centre, Åbo Akademi University, Åbo-Turku, 20500, Finland

ARTICLE INFO

Handling editor: Manel del Valle

Keywords:

Therapeutic drug monitoring
Methotrexate
Reagentless sensor
Electrochemical impedance spectroscopy
Carbon nanotube network

ABSTRACT

Ensuring effective monitoring of methotrexate (MTX) levels in the bloodstream of cancer patients undergoing high-dose methotrexate chemotherapy is crucial to prevent potentially harmful side effects. However, the absence of portable analytical devices suitable for point-of-care bedside monitoring has presented a significant obstacle to achieving real-time MTX monitoring. In this study, we developed an impedimetric immunosensor that doesn't require reagents for measuring MTX levels in undiluted human blood serum. This reagentless approach simplifies the assay process, enabling rapid and straightforward MTX quantification. The immunosensor transducer was fabricated by electrodeposition of conductive network of porous multiwalled carbon nanotube@polypyrrole/polytyramine on screen-printed gold microchip electrode (SP-Au/MWCNT₇₀@PPy-PTA). Polyclonal anti-MTX antibodies were immobilized on the film, acting as the immunorecognition element. Non-specific binding was prevented by blocking the transducer interface with denatured bovine serum albumin (dBSA) fibrils, resulting in SP-Au/MWCNT₇₀@PPy-PTA/anti-MTX_{Ab}|dBSA film electrode. When MTX binds to the SP-Au/MWCNT₇₀@PPy-PTA/anti-MTX_{Ab}|dBSA interface, the film conductance and electron transfer resistance changes. This conductivity attenuation allows for electrochemical impedimetric signal transduction without a redox-probe solution. The electrochemical impedance spectroscopy (EIS) results showed increased charge transfer resistance and phase angle as MTX concentrations increased. The SP-Au/MWCNT₇₀@PPy-PTA/anti-MTX_{Ab}|dBSA demonstrated high sensitivity, with a linear response from 0.02 to 20.0 μ M and a detection limit of 1.93 nM. The detection limit was 50 times lower than the intended safe level of MTX in human serum. The immunosensor exhibited minimal cross-reactivity with endogenous MTX analogs and serum proteins. The SP-Au/MWCNT₇₀@PPy-PTA/anti-MTX_{Ab}|dBSA immunosensor presents a simple and rapid method for therapeutic drug monitoring compared to traditional immunoassay systems.

1. Introduction

Methotrexate (2,4-diamine-N-10-methylpteroyl glutamic acid, MTX) is a folate derivative and an antimetabolite that inhibits the activity of an enzyme called dihydrofolate reductase (DHFR). DHFR is crucial for the *de novo* synthesis of nucleic acid precursors and cell proliferation [1,2]. By interfering with DHFR, MTX suppresses immune system hyperactivity and disrupts the division and growth of cancer cells [2]. Therefore, MTX is widely used as a potent immunosuppressant, anti-inflammatory

and antitumor drug. High-dose MTX (≥ 500 mg m⁻²) is a highly effective chemotherapy option for various cancers, while a lower dose (7.5–20 mg per week) is used to treat inflammatory autoimmune diseases such as rheumatoid arthritis and psoriasis [3]. However, MTX can lead to severe and life-threatening side effects, including acute kidney injury, mucositis, and multiple organ failures when used in high concentrations or for an extended period [4]. Also, due to variations in how MTX is metabolized by different individuals' body systems and its steep dose-response relationship, some patients may not derive optimal therapeutic benefits,

* Corresponding author.

** Corresponding author.

E-mail addresses: omotayo.adeniyi@umu.se (K.O. Adeniyi), solomon.tesfalidet@umu.se (S. Tesfalidet).

<https://doi.org/10.1016/j.talanta.2023.125316>

Received 21 April 2023; Received in revised form 3 October 2023; Accepted 13 October 2023

Available online 16 October 2023

0039-9140/© 2023 The Authors. Published by Elsevier B.V. This is an open access article under the CC BY-NC-ND license (<http://creativecommons.org/licenses/by-nc-nd/4.0/>).

while others may experience potentially life-threatening toxicity from a specific dose [5]. Monitoring the concentration of MTX in the blood-stream during treatment is crucial to ensure the effectiveness of high-dose MTX (HD-MTX) chemotherapy while minimizing its harmful side effects. This monitoring process, known as therapeutic drug monitoring (TDM), enables personalized dosage adjustments tailored to each patient's needs. It also helps guide the use of leucovorin (LV) rescue therapy to counteract the toxic side effects of MTX [6]. The targeted safe blood serum concentrations for MTX are 10.0 μM after 24 h, 0.10 μM at 72 h, and 0.01 at 96 h after intravenous drug administration [7,8].

Currently, TDM of MTX is conducted using traditional analytical methods like high-performance liquid chromatography-tandem mass spectrometers [9,10], fluorescence bioassays [11–13], surface-enhanced Raman spectroscopy [14–16], and various enzyme-linked immunoassay kits [8,17,18]. However, these methods require specialized laboratory setups, sample preparation, and expensive equipment, limiting their usage to centralized laboratories. Additionally, they often have a lengthy turnaround time, which is unsuitable for timely dosage adjustments. These methods are not applicable in point-of-care settings, such as bedside in hospitals or the doctor's office. Therefore, there is a need for a rapid, cost-effective, and miniaturized diagnostic device that enables point-of-care TDM of MTX. Such a device would allow healthcare professionals to monitor MTX concentrations quickly and accurately, facilitating personalized chemotherapy regimens tailored to each patient's needs.

Electrochemical impedance spectroscopy (EIS) utilizing printed electrodes is the cutting-edge technology for developing rapid point-of-care (POC) diagnostics devices. EIS immunosensors offer advantages, including simplified equipment miniaturization, low fabrication cost, minimal electric power requirement, high sensitivity, and label-free sensing [19]. In a conventional faradaic EIS immunosensor, the transducer signal detects changes in the charge transfer process between the redox probing electrolyte solution and the immunoelectrode interface upon analyte binding. However, the need for a redox probe electrolyte solution adds operational complexity and limits their real-time measurement capability [20]. Electrochemical impedance-derived capacitive spectroscopy (ECS) has recently emerged as a reagentless immunosensor that eliminates the need to add redox probe solutions [21,22]. These immunosensors involved immobilizing redox-active molecules such as ferrocene [23–25], Prussian blue [22], and redox-active polymer film [20] onto the transducer interface. ECS operates by detecting changes in the redox density-of-state of the surface-bound redox-active probes and the electron charge transfer to the electrode surface upon selective binding of the target analyte to the immunosensor interface. However, ECS has drawbacks related to the poor voltammetric and capacitive stability of the immobilized redox probes [20,26] and the high signal interference caused by biofouling of the interface in complex biological media such as blood serum. Therefore, there is significant interest in developing non-faradaic EIS immunosensors to overcome the challenges of faradaic EIS systems. Our group has recently reported several non-faradaic immunosensors that quantify serological MTX concentration using immittance spectroscopy and multivariate data analysis [27–30]. This method measures changes in the capacitive signal resulting from the variation in charge distribution and local conductance when MTX binds to the immobilized anti-MTX antibody. However, under physiological conditions with high ionic strength (100–200 mM), the Debye length (≤ 1 nm) [31] is shorter than the length of the anti-MTX antibody (10–15 nm). As a result, when MTX binds to the immobilized anti-MTX, it does not alter the capacitive signal of the immunosensor. This Debye length screening effect and the non-specific binding of other species in human blood serum limit the selectivity and sensitivity of non-faradaic capacitive immunosensors for direct detection of MTX in clinical samples. Therefore, there is a pressing need for a highly sensitive and accurate reagentless immunosensor that operates without a redox probe, exhibits low biofouling propensity, and can detect MTX in human blood serum without dilution.

To address this need, we present a new reagentless EIS immunosensor in this work. It is based on changes in the conductance or resistance of an interconnected conductive network film of anti-MTX antibody-functionalized MWCNT@PPy when MTX binds specifically to the film. The fabrication process involves creating a porous three-dimensional (3D) conductive hybrid film of multi-walled carbon nanotube-coated polypyrrole-polytyramine (MWCNT@PPy-PTA) through electrodeposition on a screen-printed gold microchip (SP-Au). The SP-Au/MWCNT₇₀@PPy-PTA/anti-MTX| α BSA immunosensor possesses several vital features that offer advantages over other EIS sensors: (i) the interconnected MWCNT₇₀@PPy-PTA network film provides excellent electrical conductivity that enhances immunosensor sensitivity; (ii) the porous 3D structure of the film facilitates a longer Debye screening length, enabling detection in human serum; (iii) the use of amyloid BSA fibrils (α BSA) minimize non-specific binding in blood serum, reducing interferences; and (iv) the incorporation of anti-MTX-antibodies ensures high specificity and accurate quantification. The fabrication steps and characterization of the film are reported. Non-faradic electrochemical impedance spectroscopy was used to detect and quantify the level of MTX in blood serum. The immunosensor operates without redox probe reagents and exhibits a low biofouling propensity, making it suitable for efficient point-of-care monitoring of MTX in blood serum. The developed SP-Au/MWCNT₇₀@PPy-PTA/anti-MTX| α BSA has demonstrated accurate detection of MTX within the clinically relevant reference range in human blood serum samples without sample dilution, making it solution for real-time and low-cost bedside TDM of MTX in clinical settings.

2. Experimental

2.1. Reagents and materials

Anti-methotrexate polyclonal antibody (MTX_{Ab}, PA5-98434) was purchased from Invitrogen by Thermo Fisher Scientific. Human Serum, AB plasma (MFCD00165829), Methotrexate hydrate (MTX, ≥ 99.0 % HPLC grade), multi-walled carbon nanotube (MWCNT, ≥ 98 % carbon basis, OD x L 6–13 nm x 2.4–20 μm), pyrrole (Py, ≥ 98 % purity), Bovine serum albumin (BSA, 99 %, fatty acid, IgG and globulin free), Sulphuric acid (H₂SO₄), Glutaraldehyde (GA, 25 % in H₂O) and tyramine hydrochloride (TA, 98 %) were obtained from Sigma-Aldrich. Phosphate-buffered saline solution (pH 7.4, 10.0 mM) was prepared following the method previously reported by Adeniyi et al. [32]. Milli-Q water with a resistivity of 18.2 M Ω cm was obtained from the Q-POD® Millipore water system. Disposable screen-printed chips (SPCEs) consisting of a printed gold ink working electrode, printed silver ink pseudo-reference electrode, and printed gold ink counter electrode deposited on a ceramic substrate were purchased from DropSens (model 220AT).

2.2. Apparatus and instruments

The surface morphology was examined on a Carl Zeiss Merlin GmbH field-emission scanning electron microscopy (FE-SEM) operated at 15.0 kV. Raman spectra of the modified surfaces were recorded with a 405 nm solid-state laser on a Renishaw Qontor spectrophotometer equipped with a confocal microscope. Contact angle (Θ) measurements were performed using an Ossila contact angle Goniometer. The DC dry state conductivity of the surfaces was recorded with an Osila four-probe instrument (T2001A3) using the van der Pauw method following the ASTM standard F84-99 [33]. The conductivity and resistivity were recorded in the X-Z direction at a probe spacing of 0.1 mm. All electrochemical experiments were performed using a Modulab potentiostat (Solartron Analytical, UK) in a three-electrode configuration at room temperature.

2.3. Fabrication of SP-Au/MWCNT₇₀@PPy-PTA/anti-MTX_{Ab}|_dBSA

The MWCNTs were purified and oxidized (ox-MWCNT) using our previously reported method [34]. To prepare the ox-MWCNTs aqueous solution, different weight percentages (20 %, 50 %, 70 %, and 80 % wt./v) of corresponding MWCNTs (0.2, 0.5, 0.7, and 0.8 mg) were dispersed in 1.0 ml of deionized water and sonicating for 2 h. The MWCNT₇₀@PPy was electrodeposited on the screen-printed gold (SP-Au) microchip by dropping a mixed solution of pyrrole (1.50 μ L, 0.2 mol L⁻¹) and ox-MWCNT (70 % wt./v, 48.50 μ L) onto the SP-Au electrode, followed by applying a constant potential of 0.65 V (vs. Ag/AgCl) for 80 s. The SP-Au/MWCNT@PPy with different weight percentages of MWCNTs (20 %, 50 %, and 80 %) were also prepared using the same method. The SP-Au/MWCNT@PPy was immersed in tyramine (10 mmol, 1.37 mg) dissolved in a 1:9 mixture of ethanol and phosphate-buffered solution (PBS, pH 7.2), then a CV was performed by cycling the potential between +0.4 and +1.2 V (vs. Ag/AgCl) at a scan rate of 50 mV s⁻¹ to form a polytyramine thin film-modified SP-Au/MWCNT₇₀@PPy-PTA electrode. The SP-Au/MWCNT₇₀@PPy-PTA electrode was washed with PBS (pH 7.2) to remove the adsorbed monomer.

2.4. Biofunctionalization of SP-Au/MWCNT₇₀@PPy-PTA with anti-MTX|_dBSA

The SP-Au/MWCNT@PPy-PTA electrode was treated with a 7 % glutaraldehyde (GA) solution at room temperature for 1 h. The GA-derivatized SP-Au/MWCNT@PPy-PTA was then incubated in an anti-MTX antibody solution (10.0 μ L, 20.0 μ g mL⁻¹) in PBS (pH 7.4) for 6 h to create SP-Au/MWCNT₇₀@PPy-PTA/anti-MTX_{Ab} immunoelectrode. Separately, 1.0 ml of BSA solution (5.0 mg mL⁻¹ in PBS buffer, pH 7.4) was heated at 90 °C for 10 min to induce the denaturing and formation of amyloid BSA fibrils (_dBSA) [35,36]. The _dBSA solution was cooled to room temperature and sonicated for 20 min. The SP-Au/MWCNT₇₀@PPy-PTA/anti-MTX_{Ab} immunoelectrode was further incubated in the _dBSA solution at room temperature for 3 h, allowing the amine groups of _dBSA to crosslink with the unreacted GA on the immunoelectrode and block the non-specific binding sites. Finally, the SP-Au/MWCNT₇₀@PPy-PTA/anti-MTX_{Ab}|_dBSA immunoelectrode was stored at 4 °C.

2.5. Quantification of MTX in huma blood serum

A standard stock solution of MTX (20.0 μ M) was prepared by dissolving MTX (1.0 mg) in 10 mL of human blood serum. Varying concentrations of MTX were prepared by further diluting the stock solution with human serum. Before the assay, the EIS signal of the SP-Au/MWCNT₇₀@PPy-PTA/anti-MTX_{Ab}|_dBSA was recorded to acquire the sensor background signal (S_0). It was then incubated with 50.0 μ L of MTX-spiked human serum sample for 5 min at room temperature, and the electrochemical impedance spectroscopy (EIS) was recorded. EIS was carried out using a potentiostat configuration with a screen-printed electrode electrochemical cell setup. Impedance data were recorded between 100 kHz and 0.5 Hz with a sinusoidal modulation amplitude voltage of 10 mV at a potential of 0.0 V (vs. Ag|AgCl pseudo-reference electrode). The impedance data were represented in Nyquist and Bode plots and analyzed with an equivalent circuit model using the Fit and simulation software [37]. The fitted EIS data were accepted if they had a high goodness-of-fit with an error of less than 0.05 % for all circuit elements. The changes in the transfer resistance and capacitance of the immunoelectrode were used to monitor the immunosensing signal. The immunosensor signal (S) in the presence of MTX (S_{MTX}) was normalized with the background signal (S_0), as $S = \frac{S_{MTX} - S_0}{S_0}$ to eliminate batch-to-batch variations of the sensor. The limit of detection (LoD) and limit of quantification (LoQ) were calculated as the signal that

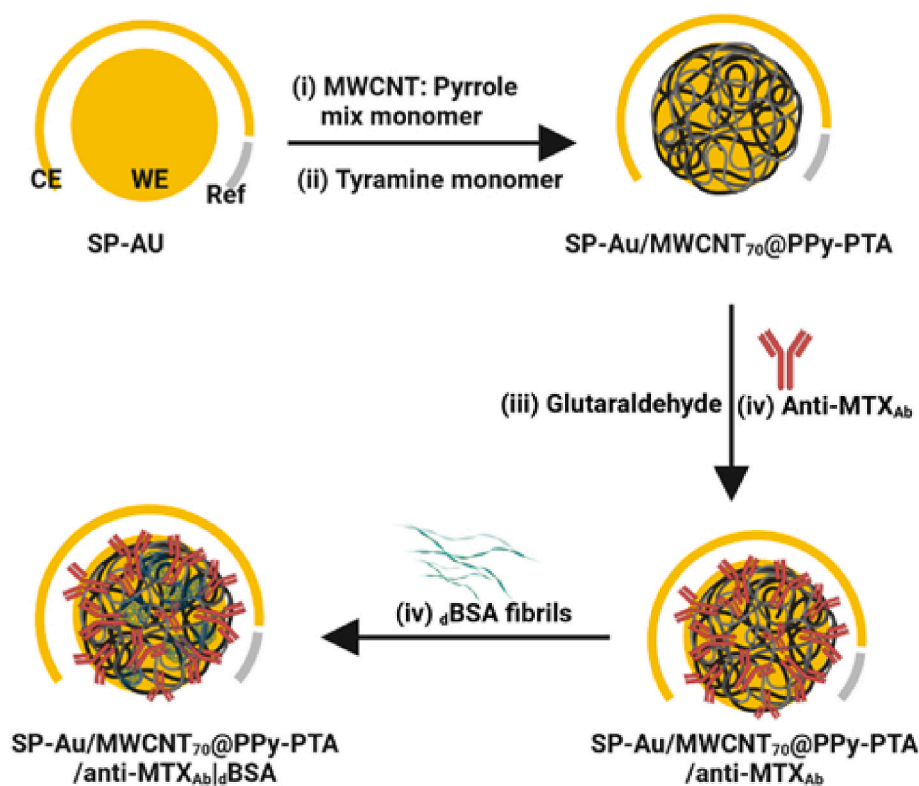
corresponds to $3S_0/\text{sensitivity}$ and $10S_0/\text{sensitivity}$ respectively.

3. Results and discussion

3.1. Fabrication of SP-Au/MWCNT₇₀@PPy/PTA/anti-MTX_{Ab}|_dBSA

The schematic illustration of the fabrication of the SP-Au/MWCNT₇₀@PPy/PTA/anti-MTX_{Ab}|_dBSA immunosensor is shown in Scheme 1. The first step involved the electrodeposition of a network of multi-walled carbon nanotubes coated with polypyrrole (MWCNT₇₀@PPy) onto a screen-printed gold (SP-Au) microchip electrode. Additionally, the electrodeposition of PPy onto SP-Au and different weight ratios of MWCNT were compared. To create abundant amine groups for anti-MTX antibody immobilization, an ultrathin polytyramine (PTA) film was electrodeposited onto the SP-Au/MWCNT₇₀@PPy film using voltammetric cycling in a tyramine monomer solution. The anti-MTX_{Ab} was covalently immobilized via glutaraldehyde-mediated crosslinking between the pedant ethylamine groups of SP-Au/MWCNT₇₀@PPy-PTA and the N-terminus polypeptide chains of anti-MTX_{Ab} to fabricate the SP-Au/MWCNT₇₀@PPy-PTA/anti-MTX_{Ab}. The residual glutaraldehyde groups and non-specific binding sites were blocked with the denatured amyloid-like BSA protofibrils (_dBSA) to form SP-Au/MWCNT₇₀@PPy-PTA/anti-MTX_{Ab}|_dBSA immunosensor. The preparation of BSA amyloid fibrils as efficient antifouling blocking agents has been previously reported [36,38].

Fig. 1 shows the cyclic voltammograms (CV) presenting the electrodeposition of SP-Au/PPy and SP-Au/MWCNT@PPy onto the SP-Au electrode from their respective monomer solutions at a scan rate of 20 mV s⁻¹. The CV confirmed the irreversible electrodeposition of PPy (Fig. 1a) and MWCNT@PPy (Fig. 1b) onto the SP-Au electrode, resulting in the formation of SP-Au/PPy and SP-Au/MWCNT@PPy polymeric films. The anodic oxidation current density increases rapidly at an onset potential of 0.45 V (vs. Ag|AgCl) during the first and subsequent CV scans, indicating the oxidation of the pyrrole monomer into radical cations and electrodeposition of PPy onto the SP-Au electrode at a higher potential [39]. The higher anodic current density observed during the reversed cathodic scans confirms the formation of an electrically conductive polymeric film. Incorporating MWCNT did not affect the electrodeposition potential of PPy. However, it resulted in a higher current density (Fig. 1b). The voltammetric current density during the electrodeposition of SP-Au/MWCNT@PPy was 30 times higher than that of SP-Au/PPy, which can be attributed to the larger electroactive surface area and higher electrical conductivity of the MWCNT@PPy film. It is worth noting that the electrodeposition of MWCNT alone was unsuccessful without the pyrrole monomer, suggesting that electrostatic and π - π bond interactions between the MWCNT and PPy facilitated the electrodeposition of MWCNT@PPy onto the SP-Au electrode. Additionally, the repetitive CV scans for the SP-Au/PPy electrodeposition showed a broad anodic and cathodic redox peak centered at 0.04 V and 0.03 V, respectively (inset, Fig. 1a'). These redox peaks were attributed to the oxidation and reduction of the deposited PPy film by counter-anions ingress and expulsion [40]. The increase in the anodic and cathodic peak currents density (inset, Fig. 1a') indicated the growth of the PPy film as the number of CV scans increased [41]. However, the voltammetric redox peak current did not significantly increase with the increasing number of CV scans for the SP-Au/MWCNT@PPy electrodeposition (inset, Fig. 1b'), suggesting the formation of MWCNT@PPy thin film that does not grow into a thick layer on subsequent scans. During the deposition using CV, MWCNT@PPy was deposited on both the SP-Au working and counter electrodes, as shown in Fig. S1, (ii). To address this issue, constant potential electrodeposition at 0.65 V vs. Ag|AgCl was successfully applied for fabricating SP-Au/PPy and SP-Au/MWCNT@PPy without affecting the SP-Au counter electrode as shown in Fig. S1, (iii). The current-time transient curve of the electrodeposition of PPy and MWCNT@PPy (Fig. 1c) showed an increased current density during the first 3 s (zone Z₁), which is due to the pyrrole



Scheme 1. Schematic illustration of the SP-Au/MWCNT₇₀@PPy-PTA/anti-MTXAb|dBSA immunosensor fabrication.

monomer oxidation to radical cations and characteristic double layer charging of the Au surface. The subsequent decrease in current density (zone Z₂, Fig. 1c, i) indicates the nucleation and progressive growth of a compact SP-Au/PPy film with reduced conductivity (zone Z₃). However, for SP-Au/MWCNT@PPy, the current density increases progressively in zones Z₂ and Z₃, indicating the formation of a continuous interconnected conductive SP-Au/MWCNT@PPy network. The current density increases gradually with the increase (%wt) of MWCNT and remains constant after 70%wt of MWCNT in SP-Au/MWCNT₇₀@PPy (Fig. 1c). The CV in Fig. S2 confirmed the electrode position of polytyramine (PTA) onto the SP-Au/MWCNT₇₀@PPy. The broad anodic peak with a maximum at 0.85 V (vs. Ag|AgCl) with no associated cathodic peaks in Fig. S2 (i), indicate irreversible oxidation of the phenoxide ions to free radical intermediate without forming reduced species. A significant decrease in the anodic peak current after the first voltammetric scan showed the self-limiting growth of polytyramine [42] and confirmed the formation of an ultrathin polytyramine film (SP-Au/MWCNT₇₀@PPy-PTA).

3.2. Structural characterization of the immunosensor interfaces

The scanning electron microscope (SEM) images (Fig. 2) confirmed differences in the morphology of the fabricated working electrode surfaces. The SP-Au showed a continuous rough gold thick film layer with numerous nanopores (Fig. 2a). A compact layer of aggregated globular PPy particles with a smooth surface was electrodeposited onto the SP-Au in the absence of MWCNT in the SP-Au/PPy film (Fig. 2b). The SEM image of SP-Au/MWCNT₁₀@PPy and SP-Au/MWCNT₂₀@PPy showed a mixture of globular and elongated irregular particles (Fig. S3), indicating the doping of MWCNT into the PPy at lower %wt. of MWCNT. Interconnected MWCNT@PPy nanotubes with smaller-sized spherical nanoparticles attached to their surfaces were obtained for the SP-Au/MWCNT₅₀@PPy (Fig. S3c). The SP-Au/MWCNT₇₀@PPy formed highly interlinked three-dimensional porous nanotube networks with smooth walls and closed-up terminal nodes (Fig. 2c). The SP-Au/

MWCNT₇₀@PPy has a core-shell morphology in which each multi-walled carbon nanotube is wrapped with a thin PPy layer, bridging the gaps between the nanotube junctions. The uniform PPy shell of MWCNT₇₀@PPy confirmed good interfacial contact between the MWCNT core and the PPy shell. The Y-shaped structure in the SP-Au/MWCNT₇₀@PPy/anti-MTXAb|dBSA confirms the successful immobilization of anti-MTXAb (Fig. 2d). The SEM image showed that the immobilized anti-MTXAb was well-spaced on the MWCNT@PPy nanotube network without crowding and aggregation.

The Raman spectra of the different modified surfaces are shown in Fig. S4. The bands at 1594 cm⁻¹ (C=C stretching), 1397 cm⁻¹ (C-N, C-C), and 1255 cm⁻¹ (C-H in-plane bending) in the spectra of SP-Au/PPy (Figs. S4 and b) and the SP-Au/MWCNT₇₀@PPy (Figs. S4 and c) are due to the vibrations of the PPy backbone carbon structure, confirming the electrodeposition of PPy. The bands at 924 (di-polaron) and 980 cm⁻¹ (polaron) are attributed to ring deformation. In contrast, the band at 1054 cm⁻¹ is assigned to C-H in-plane deformation of the PPy, respectively. The Raman bands at 1594 cm⁻¹ (G-band) and 1408 cm⁻¹ (D-band) became broader, with decreased relative peak intensity, and were shifted to lower wavenumbers with increasing %wt of MWCNT in SP-Au/MWCNT@PPy (Fig. S4, b-d). This confirms the interfacial π - π interaction between the PPy and MWCNT. The D-band (Sp³) to G-band (Sp²) ratios increased from 0.66 for SP-Au/PPy to 0.78 for SP-Au/MWCNT₇₀@PPy indicating formation π -conjugated system (Sp² character) and correlates to higher electrical conductivity. The attenuation of the intensity of the Raman bands of SP-Au/MWCNT₇₀@PPy-PTA/anti-MTXAb|dBSA (Figs. S4 and e) confirms the covalent immobilization of MTXAb.

The wettability of the different modified sensor chip surfaces was measured by recording the static contact angle (Θ) of a 5 μ L of a water droplet (Fig. 3). The SP-Au electrode was found to be hydrophobic, displaying a contact angle (Θ) of $86 \pm 1.7^\circ$ (Fig. 3a). Hydrophobic surfaces tend to repel water and have a higher propensity for non-specific adsorption of organic biomolecules. On the other hand, the contact angle of the SP-Au/PPy exhibited a lower contact angle of $46 \pm$

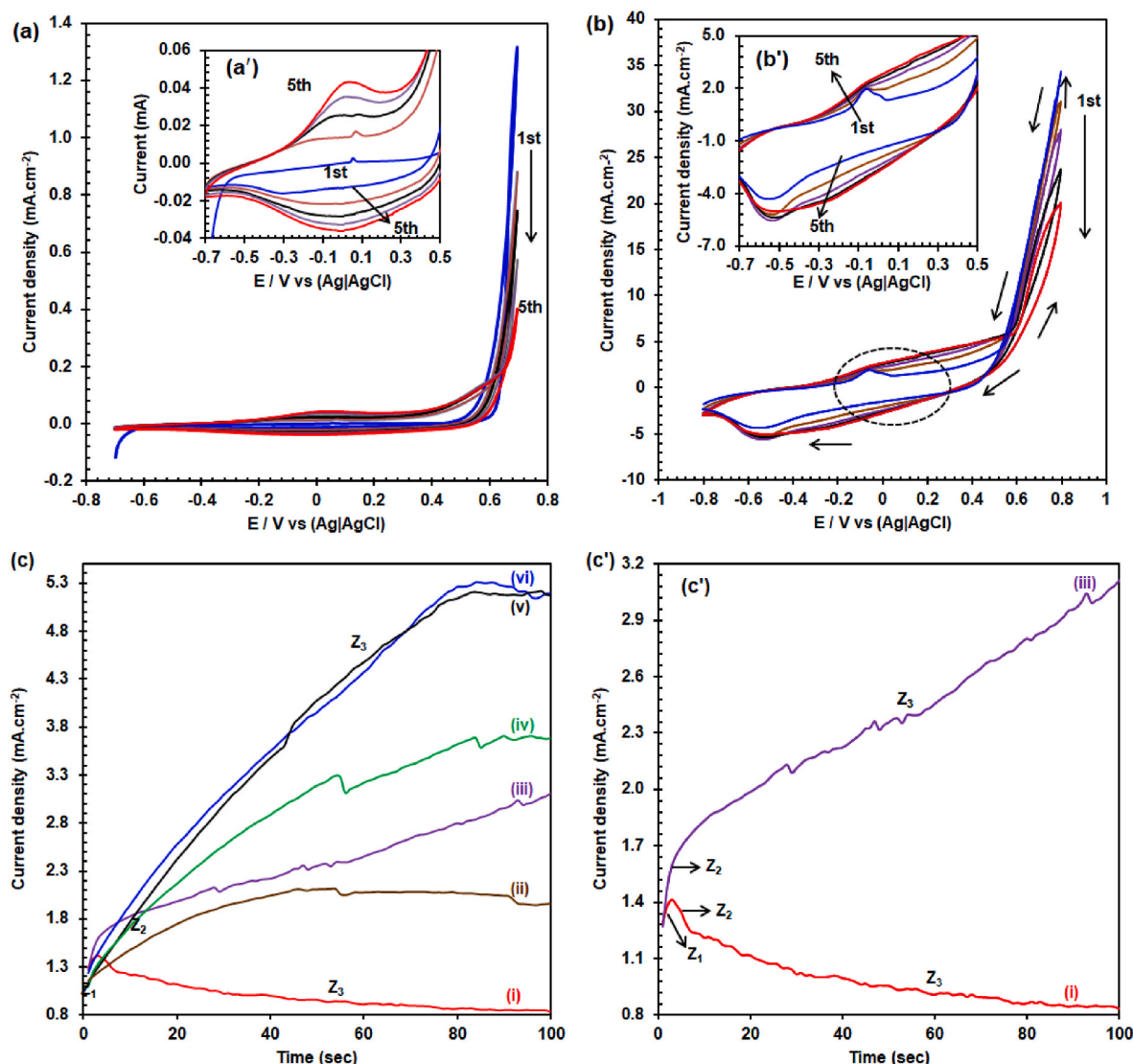


Fig. 1. Cyclic voltammograms obtained during electrodeposition of (a) SP-Au/PPy and (b) SP-Au/MWCNT@PPy in an aqueous monomer solution. (c) Current time transit curve for the fabrication of (i) SP-Au/PPy, (ii) SP-Au/MWCNT₁₀@PPy, (iii) SP-Au/MWCNT₂₀@PPy, (iv) SP-Au/MWCNT₅₀@PPy, (v) SP-Au/MWCNT₇₀@PPy and (vi) SP-Au/MWCNT₈₀@PPy. (c') is an expanded view of (c).

2.6°, indicating improved hydrophilicity due to the deposited PPy film. As the content of MWCNTs increased, the deposited film became more hydrophilic. The contact angle of SP-Au/MWCNT₇₀@PPy-PTA/anti-MTX_{Ab} was $24 \pm 6.2^\circ$, which further decreased to $16 \pm 3.7^\circ$ after blocking with dBSA (SP-Au/MWCNT₇₀@PPy-PTA/anti-MTX_{Ab}|dBSA). This indicates that the SP-Au/MWCNT₇₀@PPy-PTA/anti-MTX_{Ab}|dBSA possesses higher hydrophilicity and is less susceptible to non-specific bioaccumulation and adsorption of organic biomolecules. The lower contact angle signifies better wettability of the surface, reduced surface defects, enhanced shear forces, prevention of biofilm formation, and non-sticky surface [43], all of which contribute to the anti-biofouling capability of the SP-Au/MWCNT₇₀@PPy-PTA/anti-MTX_{Ab}|dBSA.

3.3. Electrochemical characterization of immunosensor interfaces

The electrical conductivity of the electrodeposited films was characterized using the direct current (DC) electrical probe method. The electrical conductivity of the SP-Au/PPy was 3.21×10^6 S/m with a film resistance of 63.2 Ω/sq. An increase in the percentage by weight of MWCNTs in the SP-Au/MWCNT@PPy film resulted in decreased film resistance and increased conductance (Table S1). The MWCNT within

the film provides efficient pathways for electron transfer due to their one-dimensional structure and high electron mobility, reducing the overall film resistance. The conductive paths are established through physical contact and charge transfer between the MWCNTs core and the PPy shell. The highest electrical conductivity of the SP-Au/MWCNT₇₀@PPy (2.45×10^9 S/m) confirmed that the well-ordered, highly crosslinked porous network of MWCNT₇₀@PPy enhances efficient electron transport. The interconnected MWCNT₇₀@PPy core-shell allows for ballistic electron tunneling and hopping through the walls of the MWCNT and across the nanogaps and junctions within the SP-Au/MWCNT₇₀@PPy film. The increase in the sheet resistance and decreased film conductance of SP-Au/MWCNT₇₀@PPy-PTA (1.54×10^8 S/m) compared to SP-Au/MWCNT₇₀@PPy indicate the formation of a semi-conductive film after the electrodeposition of PTA. Also, the covalently immobilized anti-MTX_{Ab} via the glutaraldehyde crosslinking induced an electrostatic gating effect [44] that altered the electric field around the SP-Au/MWCNT₇₀@PPy-PTA. This gating effect decreases the electrical conductivity of the SP-Au/MWCNT₇₀@PPy-PTA/anti-MTX_{Ab} (2.74×10^6 S/m). There were no significant changes in the conductivity of the SP-Au/MWCNT₇₀@PPy/anti-MTX_{Ab}|dBSA (2.3×10^6 S/m), indicating blocking non-specific sites with denatured BSA amyloid fibrils did not

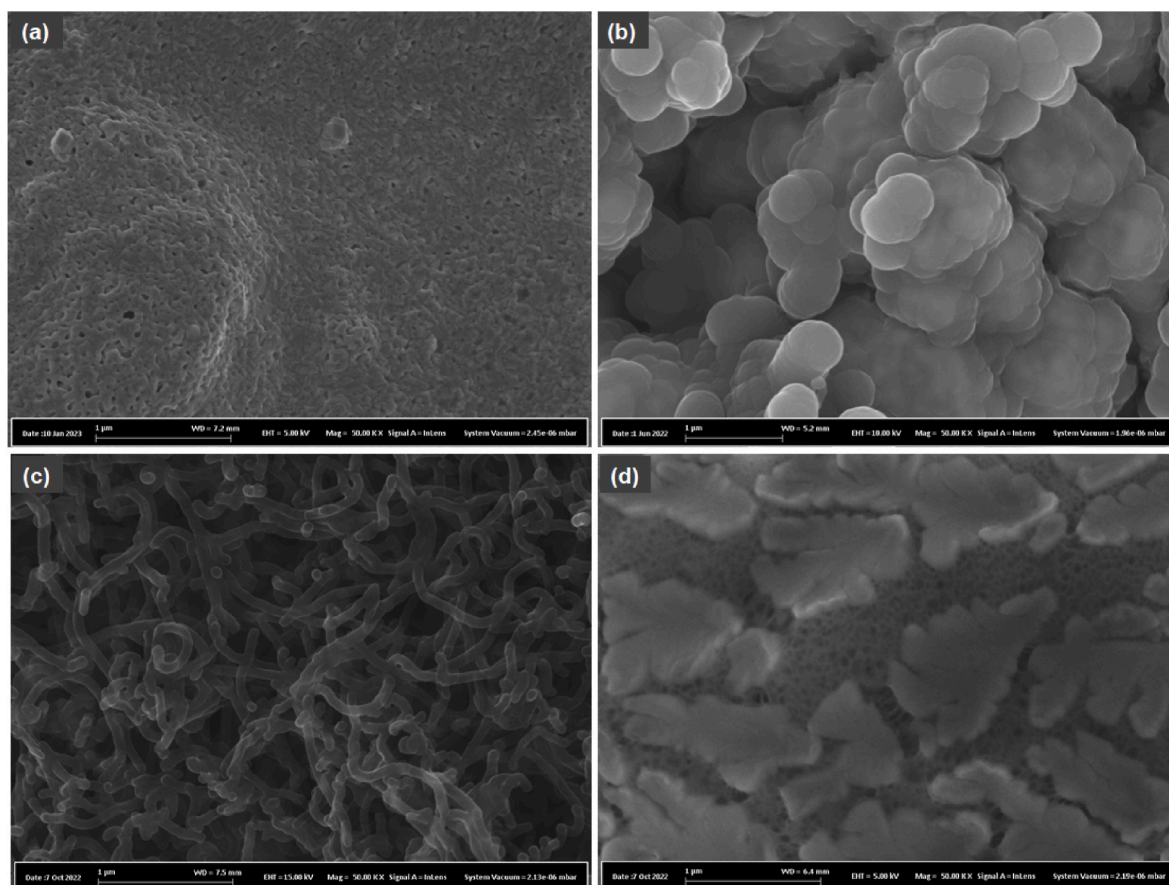


Fig. 2. SEM images of (a) SP-Au, (b) SP-Au/PPy, (c) SP-Au/MWCNT₇₀@PPy, and (d) SP-Au/MWCNT₇₀@PPy-PTA/anti-MTX_{Ab}|dBSA.

alter the film conductivity significantly.

The cyclic voltammetry measurements of SP-Au/PPy and the SP-Au/MWCNT@PPy films in PBS (pH 7.4) showed superimposable non-faradaic capacitive background current and faradaic redox current (Fig. 4a), indicating the pseudocapacitive behavior of the deposited film. The CV of SP-Au/PPy showed a quasi-reversible redox pair at 230 mV and −280 mV ($\Delta E_p = 50$ mV), attributed to the oxidation and reduction of PPy, respectively. The shift of the redox peaks to lower potential and increasing current density in Fig. 4a, (iii-iv) confirmed the higher electroactive surface area with increasing %wt. of MWCNT. The highest current density and lowest ΔE_p (24.9 mV) of SP-Au/MWCNT₇₀@PPy (Fig. 4a, v) were due to the efficient charge transport process across the interconnected film. The decrease in current density and ΔE_p of SP-Au/MWCNT₇₀@PPy-PTA/anti-MTX_{Ab}|dBSA (Fig. 4a, vi) further confirms the immobilization of anti-MTX_{Ab}|dBSA. The charge transfer properties were examined by electrochemical impedance spectroscopy (EIS). The most significant feature of the Nyquist plot (Fig. 4b) is the decrease in the diameter of the semicircle with increasing %wt of MWCNT in the electrodeposited SP-Au/MWCNT@PPy films. The EIS data were best fitted with an equivalent circuit with a film resistance (R_{CT}) parallel to the constant phase element (CPE) (inset, Fig. 4b). The R_{CT} of the SP-Au/PPy film (3.48 ± 0.3 k Ω) decreases with increasing %wt of MWCNT in the film. The SP-Au/MWCNT₇₀@PPy film had the lowest R_{CT} of 0.04 ± 0.01 k Ω , confirming that the interconnected three-dimensional porous MWCNT₇₀@PPy network promotes efficient electron transport and facilitates charge transfer within the film. The Warburg impedance in the Nyquist plot of SP-Au/MWCNT₇₀@PPy (Fig. 4b, iv) further confirmed that the interconnected porous network nanostructure facilitates efficient diffusion of ions and promotes effective mass transport within the film. The slight increase of the R_{CT} to 0.16 ± 0.5 k Ω for the SP-Au/MWCNT₇₀@PPy-PTA showed that the electrodeposition of ultrathin film

of PTA does not significantly decrease the ionic and charge transfer mobility process within the film. The covalently immobilized anti-MTX_{Ab} induced an electrostatic gating effect on the film and increased the R_{CT} of SP-Au/MWCNT₇₀@PPy-PTA/anti-MTX_{Ab}|dBSA to 0.21 ± 0.1 k Ω .

3.4. Immunosensing principle

The sensing principle is based on the modulation of the conductance of the SP-Au/MWCNT₇₀@PPy-PTA/anti-MTX_{Ab}|dBSA film when the target analyte (MTX) binds to the immobilized biorecognition element (anti-MTX_{Ab}) to form an insulating antibody-analyte immunocomplex (SP-Au/MWCNT₇₀@PPy-PTA/anti-MTX_{Ab}-MTX|dBSA). The immunocomplex disrupts the film's conductivity by inhibiting electron tunneling and hopping transport processes. As a result, the film conductance (g_f) decreases, and its charge transfer resistance ($R_{CT} = 1/g_f$) increases, leading to a change in the electrical properties of the film. These changes in the electrical properties of the film are measured as the impedance to the alternating current output (ΔI_{out}) when an AC signal with an amplitude of 10 mV superimposed to a DC bias voltage of $V_{DC} = 0$ is applied. The AC signal changes the potential of the interface relative to the fixed potential of the Ag|AgCl pseudo-reference electrode (V_{REF}). The impedance of the immunosensor is the ratio of the alternating voltage put (V_{in}) to the output current (I_{out}) [45]. The total impedance (Z_T) is given by:

$$Z_T = \frac{\Delta V_{in}}{\Delta I_{out}} = R_s + \frac{1}{g_f + (Q_{DL})(\omega)^n} \quad (1)$$

where R_s represent the electrolyte resistance, $1/g_f = R_{CT}$ is the charge transfer resistance of SP-Au/MWCNT₇₀@PPy/anti-MTX_{Ab}|dBSA film, Q_{DL} is the constant phase element (CPE) that reflects the double-layer

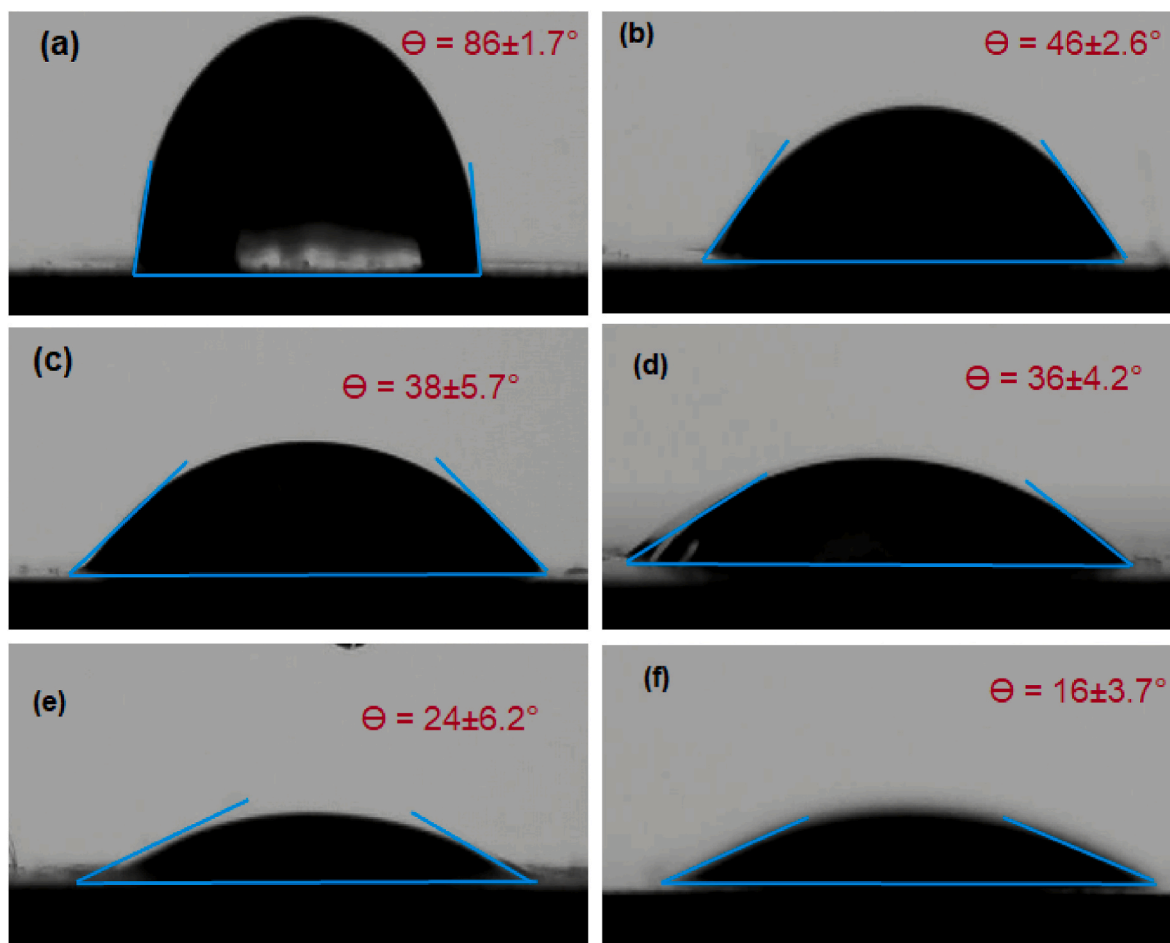


Fig. 3. Static water contact angle of (a) SP-Au, (b) SP-Au/PPy, (c) SP-Au/MWCNT₂₀@PPy, (d) SP-Au/MWCNT₅₀@PPy, (e) SP-Au/MWCNT₇₀@PPy-PTA/anti-MTX_{Ab}, and (f) SP-Au/MWCNT₇₀@PPy-PTA/anti-MTX_{Ab}|dBSA.

capacitance formed by the accumulation of ions at the electrode/electrolyte interface. j is an imaginary unit, and ω is the angular frequency. The Z_T is represented by its Euler's form as $Z_T = Z' + jZ''$ (used for plotting Nyquist plot) and by its polar form as $Z_T = |Z|e^{j\theta}$ (used for plotting Bode plot) corresponding to the non-faradaic capacitive response of the immunosensor. The Nyquist plots were fitted with an equivalent circuit having an electrolyte resistance (R_s) in series with a parallel combination of CPE and the charge transfer resistance (R_{CT}) to explore the quantitative analytical analysis of the immunosensor response.

3.5. Investigation of antibiofouling performance

The change in the sensor response ($\% \Delta R$) was used to evaluate the resistance to non-specific serum protein adsorption by comparing the charge transfer resistance before (R_o) and after (R_{MTX}) incubation with various diluted ($\% v/v$) blood serum samples (Eq. (2)).

$$\% \Delta R = \frac{R_{MTX} - R_o}{R_o} \times 100 \quad (2)$$

The background signal of the two sensor variants, SP-Au/MWCNT₇₀@PPy-PTA/anti-MTX_{Ab}, and SP-Au/MWCNT₇₀@PPy-PTA/anti-MTX_{Ab}|dBSA were compared to assess their antibiofouling performance. A lower percentage change in the film resistance of the background signal indicates antibiofouling performance. Changes in the sensor response after incubation with various dilution ratios of human blood serum are shown in Fig. S5. The signal of the SP-Au/MWCNT₇₀@PPy-PTA/anti-MTX_{Ab} (Fig. S5, blue bars) after incubation with the blood serum is due to the non-specific adsorption of the serum

proteins. The non-specific signal contributes approximately 2.6 % of the total sensor signal in undiluted human serum. This indicates that the interface without dBSA has inefficient antibiofouling capability. In contrast, the signal of the SP-Au/MWCNT₇₀@PPy-PTA/anti-MTX_{Ab}|dBSA was 0.24 % after incubation with the undiluted human serum (Fig. S5, red bars), confirming blocking with dBSA fibrils prevents non-specific serum protein adsorption. BSA fibrils are known to exhibit excellent serum biofouling properties [35,46]. SP-Au/MWCNT₇₀@PPy-PTA/anti-MTX_{Ab}|dBSA demonstrated excellent antibiofouling properties, indicating a promising potential for ultrasensitive detection in undiluted blood serum samples.

3.6. Impedimetric detection of MTX in undiluted blood serum sample

The Nyquist plot of SP-Au/MWCNT₇₀@PPy-PTA/anti-MTX_{Ab}|dBSA immunosensor in undiluted human serum without MTX showed stable baseline signals without a significant change in the diameter of the semicircle and the phase angles upon repetitive measurements. The diameter of the semicircle in the Nyquist plot, which corresponds to the transfer resistance of the film, the height of the imaginary impedance (Z'') (Fig. 5a, i), and the magnitude of the phase angle (Fig. 5c) remained unchanged in the blank samples, indicating high sensor baseline stability and low background noise. However, upon incubation with increasing concentrations of MTX (0.02–20.0 μM) in spiked human serum samples, the diameter and height of the semicircle increased progressively (Fig. 5a, ii) with increasing MTX concentrations, indicating the binding of MTX to the immobilized anti-MTX_{Ab} induced an extra resistance on the film. The Nyquist plots were analyzed using an

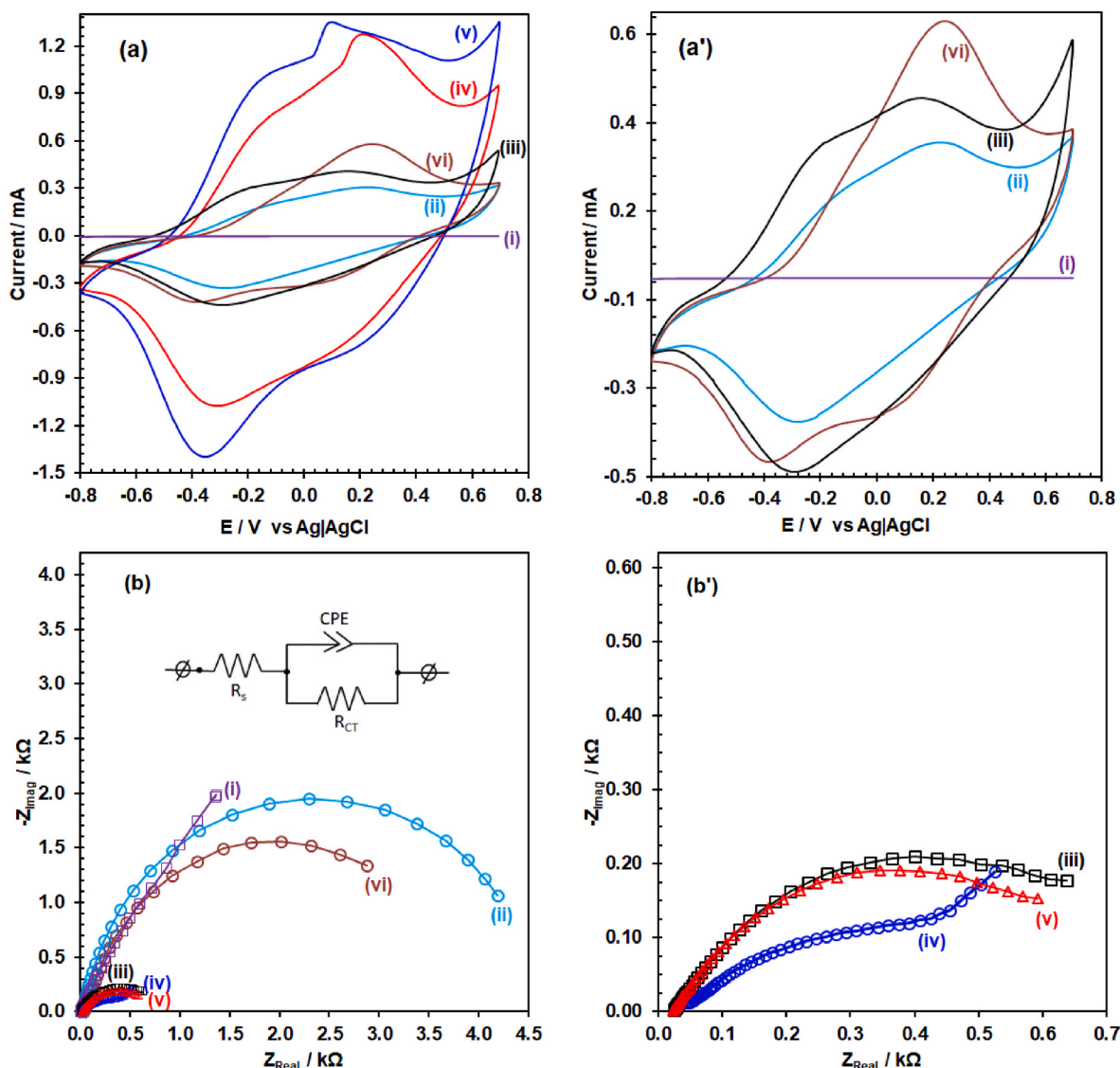


Fig. 4. (a) Cyclic voltammograms and (b) Nyquist plot of (i) SP-Au, (ii) SP-Au/PPy, (iii) SP-Au/MWCNT₂₀@PPy, (iv) SP-Au/MWCNT₇₀@PPy, (v) SP-Au/MWCNT₇₀@PPy-PTA and (vi) SP-Au/MWCNT₇₀@PPy-PTA/anti-MTX_{Ab}|dBSA. (a') and (b') are the expanded views of (a) and (b), respectively.

equivalent circuit, as depicted in the insert of Fig. 5 (a). This circuit consisted of an electrolyte resistance (R_s) in series with a parallel combination of CPE and charge transfer resistance (R_{CT}). The magnitude of the circuit elements determined through fittings was summarized in Table S2. To explore the quantitative analytical analysis of the immunosensor response, the normalized percentage changes in the magnitude of the charge transfer resistance ($\% \Delta R/R_0$) were calculated as $\% \Delta R/R_0 = (R_{CTMTX} - R_{CT0})/R_{CT0}$, where R_{CT0} and R_{CTMTX} represent the charge transfer resistance before and after immunoreaction with MTX, respectively. The dose-response curve of the change in the film resistance ($\% \Delta R/R_0$) in response to varying MTX concentrations was modeled using a hyperbolic curve fitting shown in Fig. 5b. This curve fitting indicates an affinitive binding of MTX to the immunosensor surface. The saturation signal, corresponding to the maximum signal of the dose-response curve, was 36.0 ± 1.5 %. The affinitive binding constant (K_D) of MTX was estimated from the fitted curve as $0.32 \mu\text{M}$. The low K_D indicates high affinitive binding of MTX to the immunosensing interface. The calibration plot (inset Fig. 5b) relating the change in the $\% \Delta R/R_0$ to the logarithm of MTX concentrations demonstrated linearity within the dynamic ranges of 0.02 – $20.0 \mu\text{M}$. The corresponding linear regression equation was determined as $(\% \Delta R/R_0) = 24.29 + 10.54 \log[\text{MTX}] (\mu\text{M})$

and the correlation coefficient (R^2) was 0.985 . Based on this analysis of the changes in film transfer resistance, the sensor exhibits a sensitivity of $84.8 \text{ } \mu\text{M} \cdot \text{cm}^{-2}$ with a limit of detection (LoD) of 1.93 nM and a limit of quantification (LoQ) of 6.11 nM of MTX, respectively. In addition, the capacitive impedance response of SP-Au/MWCNT₇₀@PPy-PTA/anti-MTX_{Ab}|dBSA to various MTX concentrations was investigated to quantify the analytical signal. The imaginary component of the complex impedance ($1/\omega Z''$) reached its maximum at a phase angle of approximately 2.7 Hz (Fig. 5c), indicating the optimum capacitive response of the SP-Au/MWCNT₇₀@PPy-PTA/anti-MTX_{Ab}|dBSA at this frequency. As the concentrations of MTX increased, there was a shift to a higher phase angle ($\Delta\phi$), which is associated with the changes in the dielectric properties of the immunosensing interface. This alteration led to a decrease in the capacitance of the immunosensor with increasing MTX concentrations (Fig. S6). The analytical curves (Fig. 4d) were obtained by plotting the normalized $\% \Delta\phi$ shift at 2.7 Hz against different concentrations of MTX. The sensor response demonstrated linearity within a dynamic range of 0.02 – $20.0 \mu\text{M}$ with a linear regression equation of $\%(\Delta\phi/\phi_0) = 8.33 + 2.66 \log[\text{MTX}] (\mu\text{M})$ and an R^2 of 0.993 . Based on the analysis of phase angle changes, the sensor's sensitivity was $21.2 \text{ } \mu\text{M}^{-1} \text{cm}^{-2}$. Using the capacitive response, the LoD and LoQ of 7.63 nM

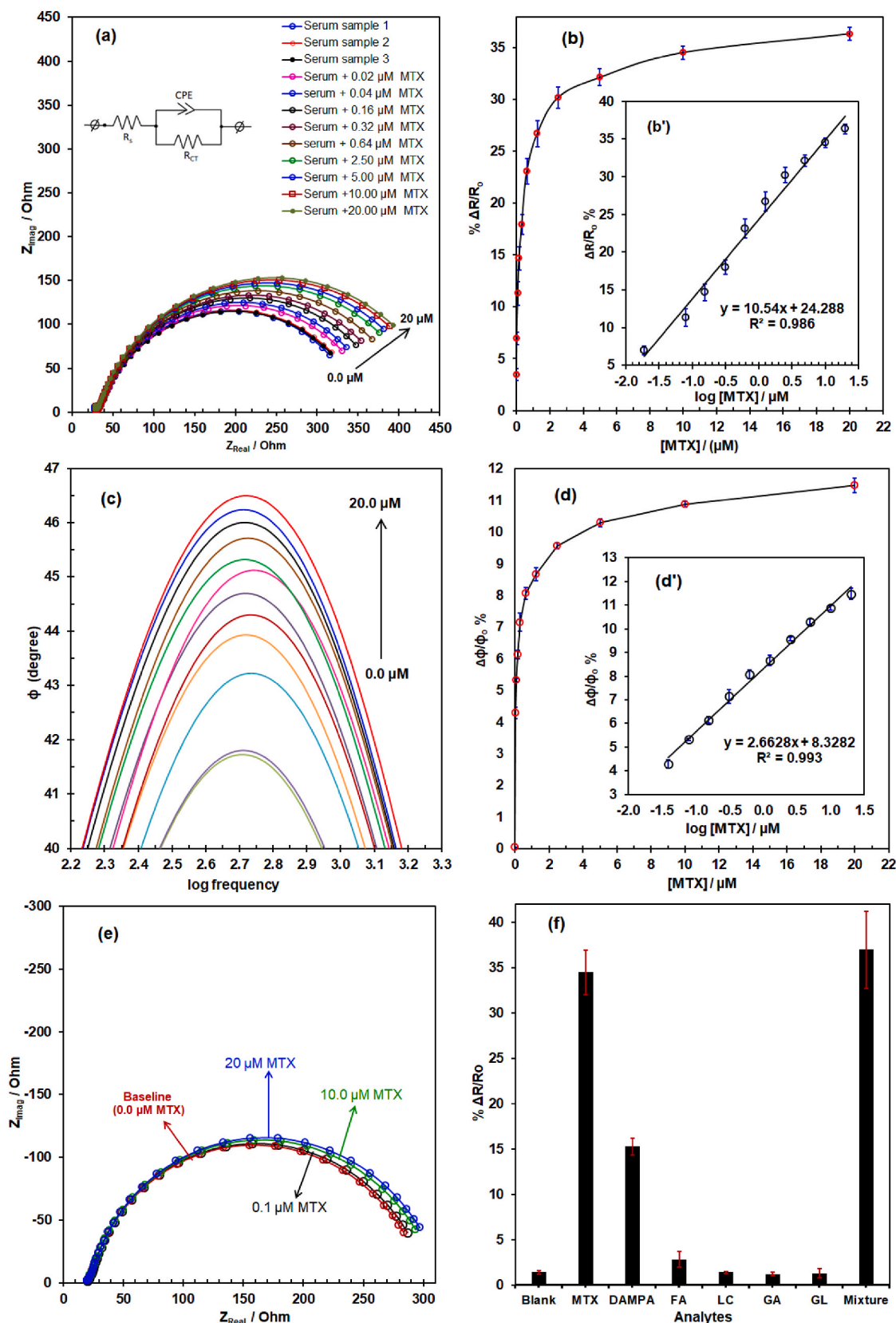


Fig. 5. impedimetric response of SP-Au/MWCNT₇₀@PPy-PTA/anti-MTXAb₄BSA: (a) Nyquist plot and corresponding, (b) dose-response curve with the inset of the linear calibration plot (b'). (c) Bode plot and corresponding (d) dose-response curve with the inset of the linear calibration plot (d'). (e) Nyquist plot of SP-Au/MWCNT₇₀@PPy-PTA/anti-MTXAb₄BSA to different concentrations of MTX. (f) SP-Au/MWCNT₇₀@PPy-PTA/anti-MTXAb₄BSA response to interfering MTX analogs. The error bar represents the standard deviation of three independent measurements.

and 23.0 nM, respectively.

The LoD and the linear concentration range of the SP-Au/MWCNT₇₀@PPy-PTA/anti-MTX_{Ab}|dBSA falls within the clinical targeted serum MTX concentrations of >5.0–10.0 $\mu\text{mol L}^{-1}$ at 24 h, 0.10 $\mu\text{mol L}^{-1}$ at 72 h, and below 0.05 $\mu\text{mol L}^{-1}$ at 96 h after intravenous MTX administration to prevent toxic side effects [8]. Compared to other MTX immunoassays listed in Table 1, the LoD of the proposed immunosensor utilizing changes in both resistivity (LoD of 1.97 nM) and capacitive components (LoD of 7.63 nM) of the signal demonstrates a lower or comparable limit of detection. The reagentless sensing mode and the ability to detect MTX without dilution showcase the superior analytical performance of the SP-Au/MWCNT₇₀@PPy-PTA/anti-MTX_{Ab}|dBSA over other sensing systems listed in Table 1. This suggests that the proposed immunosensor can potentially be a highly sensitive and accurate method for detecting MTX in blood serum samples without sample dilution. Furthermore, it offers the advantage of not requiring additional reagents and enables direct measurements in undiluted human serum samples.

3.7. Specificity, selectivity, and reproducibility

The control experiment with the SP-Au/MWCNT₇₀@PPy-PTA|dBSA electrode (without immobilized anti-MTX_{Ab}) demonstrates the immunoreaction specificity and selectivity of the sensor response (Fig. 5e). The diameter of the semicircle and change in transfer resistance (ΔR) did not change significantly after incubating with different serological MTX concentrations, indicating that non-immunospecific interaction of MTX with the SP-Au/MWCNT₇₀@PPy-PTA|dBSA resulted in minimal signal changes even at high MTX concentrations. This confirms the high immuno-specificity of the SP-Au/MWCNT₇₀@PPy-PTA/anti-MTX_{Ab}|dBSA. The cross-reactivity of SP-Au/MWCNT₇₀@PPy-PTA/anti-MTX_{Ab}|dBSA with potentially interfering endogenous MTX analogs and metabolites in blood serum was also evaluated. High concentrations (20.0 μM) of the potential interference with MTX (5.0 μM) were analyzed individually and as a mixture. The results (Fig. 5f) showed that the MTX analogs, including folic acid (FA), leucovorin calcium (LV), glutamic acid (GA), 5-fluorouracil (5-FU), and tetrahydrofolic acid (HFA), did not induce an impedimetric response and did not interfere with the accurate determination of MTX. However, 2,4-diamino-N(10)-methylpterioic acid (DAMPA), a minor metabolite of MTX, induced an immunosensor response (15.3 %), indicating cross-reactivity between DAMPA and anti-MTX antibody. Nevertheless, DAMPA is rapidly eliminated and detected only in a few patients receiving HD-TMX and is not expected to interfere with the accurate quantification of MTX in most patients [49]. Overall, the SP-Au/MWCNT₇₀@PPy-PTA/anti-MTX_{Ab}|dBSA immunosensor demonstrated excellent specificity and selectivity for detecting MTX in human serum samples. Fig. S7 shows the response of six independently prepared immunosensors to 0.5 μM of MTX. The inter-immunoassay reproducibility, indicated by the low relative standard deviation of 1.64 % among the independently prepared immunosensors, was excellent, further highlighting the reliability of the immunosensor for clinical application in high-dose MTX chemotherapy monitoring.

4. Conclusion

In summary, the developed immunosensor based on a reagentless, redox probe-free, and ultrasensitive impedimetric approach using multi-walled carbon nanotube@polypyrrole-polytyramine hybrid film on a screen-printed gold electrode has shown promising results for the monitoring of MTX level in blood serum. The optimized fabrication conditions of the SP-Au/MWCNT₇₀@PPy-PTA/anti-MTX_{Ab}|dBSA immunosensor have resulted in a highly conductive and stable sensing platform. The immunosensor has exhibited high antifouling properties, enabling accurate detection of MTX in undiluted human serum samples. The immunosensor has also demonstrated good analytical reliability

Table 1

Comparison of the analytical performance of the SP-Au/MWCNT₇₀@PPy-PTA|dBSA immunosensor with other reported methods (TW – this work).

Transducer interface	Methods	Matrix	Linear range (μM)	LoD (nM)	Ref.
SP-Au/MWCNT ₇₀ @PPy-PTA/anti-MTX _{Ab} dBSA	EIS	Serum	0.02–20	1.93	TW
	Capacitive	Serum	0.02–20	7.63	TW
Au/anti-MTX _{Ab}	EIS-MVA	PBS	2.7×10^{-4} – 27	0.16	[30]
GCE/IPA/anti-MTX _{Ab}	EIS-MVA	PBS	3.0×10^{-4} – 30	0.7	[27]
AuE-CP/anti-MTX _{Ab}	EIS-MVA	PBS	3.0×10^{-4} – 30	0.007	[29]
Gold nanopillar	SERS	Serum	1.81–5	0.55	[15]
Silver nanopillar/MTX aptamer	SERS	Serum	5–150	60	[14]
GCE/SWCNT/Nafion/DNA	SWV	PBS	0.02–1.5	8	[47]
Multiplied Enzyme immunoassay	UV–Vis	Serum	0.04–1.2	300	[48]
	UV–Vis	Serum	0.05–1	50	[18]

EIS-MVA: Electrochemical impedance spectroscopy-multivariate data analysis; SWV: square wave voltammetry; SERS: surface-enhanced Raman spectroscopy.

with acceptable reproducibility and selectivity in the presence of other interference and MTX analogs. The developed immunosensor has several advantages over other MTX immunoassays, including (i) the reagentless and label-free sensing format, (ii) the capability of accurate quantification of MTX in undiluted human blood serum sample, (iii) high sensitivity, which allows LoD (1.93 nM) which is about 50-times lower than the clinically safe reference concentration of ≤ 100 nM at 72 h, (iv) high selectivity for MTX without interference from folic acid and other MTX analogs and (v) the immunosensing system can be easily miniaturized by integrating with a hand-held electrochemical potentiostat. The results of this study indicate the excellent potential of the developed immunosensor for clinical translation and bedside point-of-care MTX monitoring, which could potentially improve patient care and treatment outcomes.

Credit author statement

Kayode Omotayo Adeniyi: Conceptualization, Methodology, Data curation, Writing – original draft. Blerina Osmanaj and Gopinathan Manavalan: Methodology, Characterization of materials, Writing – review & editing. Avni Berisha and Jyri-Pekka Mikkola: Writing – review & editing. Solomon Tesfalidet: Conceptualization, Supervision, Resources, Writing – review & editing and Funding acquisition.

Declaration of competing interest

The authors declare that they have no known competing financial interests or personal relationships that could have appeared to influence the work reported in this paper.

Data availability

No data was used for the research described in the article.

Acknowledgments

This research was funded by the Kempe Foundations, Sweden. STINT-NRF is appreciated for complementary research funding. The Umeå Centre for Electron Microscopy (UCEM) and Vibrational Spectroscopy Core Facility (ViSp) at the Chemical Biological Centre (KBC), Umeå University, is gratefully acknowledged.

Appendix A. Supplementary data

Supplementary data to this article can be found online at <https://doi.org/10.1016/j.talanta.2023.125316>.

References

- [1] Y. Bedoui, X. Guillot, J. Sélambom, P. Guiraud, C. Giry, M.C. Jaffar-Bandjee, S. Ralandison, P. Gasque, Methotrexate an old drug with new tricks, *Int. J. Mol. Sci.* 20 (2019), <https://doi.org/10.3390/ijms20205023>.
- [2] B.N. Cronstein, T.M. Aune, Methotrexate and its mechanisms of action in inflammatory arthritis, *Nat. Rev. Rheumatol.* 16 (2020) 145–154, <https://doi.org/10.1038/s41584-020-0373-9>.
- [3] P. Cipriani, P. Ruscitti, F. Carubbi, V. Liakouli, R. Giacomelli, Methotrexate: an old new drug in autoimmune disease, *Expert Rev. Clin. Immunol.* 10 (2014) 1519–1530, <https://doi.org/10.1586/1744666X.2014.962996>.
- [4] R. Niinimäki, H. Aarnivala, J. Banerjee, T. Pokka, K. Vepsäläinen, A. Harila-Saari, Reduced dose folinic acid rescue after rapid high-dose methotrexate clearance is not associated with increased toxicity in a pediatric cohort, *Support. Care Cancer* 30 (2022) 127–133, <https://doi.org/10.1007/s00520-021-06395-3>.
- [5] A. Paci, G. Veal, C. Bardin, D. Levéque, N. Widmer, J. Beijnen, A. Astier, E. Chatelut, Review of therapeutic drug monitoring of anticancer drugs part 1 - cytotoxics, *Eur. J. Cancer* 50 (2014) 2010–2019, <https://doi.org/10.1016/j.ejca.2014.04.014>.
- [6] D.M. Bach, J.A. Straseski, W. Clarke, Therapeutic drug monitoring in cancer chemotherapy, *Bioanalysis* 2 (2010) 863–879, <https://doi.org/10.4155/bio.10.48>.
- [7] K.O. Adeniyi, B. Osmanaj, G. Manavalan, A. Samikannu, J.P. Mikkola, B. Avni, J. F. Boily, S. Tesfalidet, Engineering of layered iron vanadate nanostructure for electrocatalysis: simultaneous detection of methotrexate and folinic acid in blood serum, *Electrochim. Acta* 458 (2023), 142538, <https://doi.org/10.1016/j.electacta.2023.142538>.
- [8] X. Shi, H. Gao, Z. Li, J. Li, Y. Liu, L. Li, Q. Zhang, Modified enzyme multiplied immunoassay technique of methotrexate assay to improve sensitivity and reduce cost, *BMC Pharmacol. Toxicol.* 20 (2019) 1–7, <https://doi.org/10.1186/s40360-018-0283-5>.
- [9] F. Karami, S. Ranjbar, Y. Ghasemi, M. Negahdaripour, Analytical methodologies for determination of methotrexate and its metabolites in pharmaceutical, biological and environmental samples, *J. Pharm. Anal.* 9 (2019) 373–391, <https://doi.org/10.1016/j.jppha.2019.06.001>.
- [10] W. Zhou, Y. Deng, C. Zhang, Z. Liu, J. Zhang, L. Zhou, L. Shao, C. Zhang, Current status of therapeutic drug monitoring for methotrexate, imatinib, paclitaxel in China, *Clin. Biochem.* 104 (2022) 44–50, <https://doi.org/10.1016/j.clinbiochem.2022.03.005>.
- [11] M.A. Pesce, S.H. Bodourian, Evaluation of a fluorescence polarization immunoassay procedure for quantitation of methotrexate, *Ther. Drug Monit.* 8 (1986), <https://doi.org/10.1097/00007691-198603000-00020>.
- [12] J. He, J. Wang, M. Zhang, G. Shi, Ultrasensitive therapeutic drug monitoring of methotrexate by a structure-switching aptamer with cascade primer exchange reaction, *Analyst* 148 (2022) 222–226, <https://doi.org/10.1039/d2an01658c>.
- [13] A. Mohammadzadeh, A. Jouyban, M. Hasanadeh, V. Shafiei-Irannejad, J. Soleymani, Ultrasensitive fluorescence detection of antitumor drug methotrexate based on a terbium-doped silica dendritic probe, *Anal. Methods* 13 (2021) 4280–4289, <https://doi.org/10.1039/d1ay01098k>.
- [14] Y. Göksel, K. Zor, T. Rindzevicius, B.E. Thorhaug Als-Nielsen, K. Schmiegelow, A. Boisen, Quantification of methotrexate in human serum using surface-enhanced Raman scattering—toward therapeutic drug monitoring, *ACS Sens.* 6 (2021) 2664–2673, <https://doi.org/10.1021/acssensors.1c00643>.
- [15] Y. Göksel, E. Dumont, R. Slipets, S.T. Rajendran, S. Sarikaya, L.H.E. Thamdrup, K. Schmiegelow, T. Rindzevicius, K. Zor, A. Boisen, Methotrexate detection in serum at clinically relevant levels with electrochemically assisted SERS on a benchtop, custom built Raman spectrometer, *ACS Sens.* 7 (2022) 2358–2369, <https://doi.org/10.1021/acssensors.2c01022>.
- [16] S. Fornasaro, S.D. Marta, M. Rabusin, A. Bonifacio, V. Sergio, Toward SERS-based point-of-care approaches for therapeutic drug monitoring: the case of Methotrexate, *Faraday Discuss* 187 (2016) 485–499, <https://doi.org/10.1039/c5fd00173k>.
- [17] R. Bouquie, M. Grégoire, H. Hernando, C. Azoulay, E. Dailly, C. Monteil-Ganière, A. Pineau, G. Deslandes, P. Joliet, Evaluation of a methotrexate chemiluminescent microparticle immunoassay: comparison to fluorescence polarization immunoassay and liquid chromatography-tandem mass spectrometry, *Am. J. Clin. Pathol.* 146 (2016) 119–124, <https://doi.org/10.1093/ajcp/aqw088>.
- [18] M.P. Borgman, M.F. Hiemer, A.R. Molinelli, J.C. Ritchie, S.A. Jortani, Improved sensitivity for methotrexate analysis using enzyme multiplied immunoassay technique on the Siemens Viva-E instrument, *Ther. Drug Monit.* 34 (2012) 193–197, <https://doi.org/10.1097/FTD.0b013e31824b93a5>.
- [19] B. Lucas Garrote, L.C. Lopes, E.F. Pinzón, F.C. Mendonça-Natividade, R.B. Martins, A. Santos, E. Arruda, P.R. Bueno, Reagentless quantum-rate-based electrochemical signal of graphene for detecting SARS-CoV-2 infection using nasal swab specimens, *ACS Sens.* 7 (2022) 2645–2653, <https://doi.org/10.1021/acssensors.2c01016>.
- [20] A. Baradoke, R. Hein, X. Li, J.J. Davis, Reagentless redox capacitive assaying of C-reactive protein at a polyaniline interface, *Anal. Chem.* 92 (2020) 3508–3511, <https://doi.org/10.1021/acs.analchem.9b05633>.
- [21] P.R. Bueno, F. Fabregat-Santiago, J.J. Davis, Elucidating capacitance and resistance terms in confined electroactive molecular layers, *Anal. Chem.* 85 (2013) 411–417, <https://doi.org/10.1021/ac303018d>.
- [22] P.R. Bueno, G. Mizzon, J.J. Davis, Capacitance spectroscopy: a versatile approach to resolving the redox density of states and kinetics in redox-active self-assembled monolayers, *J. Phys. Chem. B* 116 (2012) 8822–8829, <https://doi.org/10.1021/jp303700f>.
- [23] A. Santos, F.C. Carvalho, M.C. Roque-Barreira, P.R. Bueno, Impedance-derived electrochemical capacitance spectroscopy for the evaluation of lectin-glycoprotein binding affinity, *Biosens. Bioelectron.* 62 (2014) 102–105, <https://doi.org/10.1016/j.bios.2014.06.034>.
- [24] J. Cecchetti, A. Santos, A. Mondini, E.M. Cilli, P.R. Bueno, Serological point-of-care and label-free capacitive diagnosis of dengue virus infection, *Biosens. Bioelectron.* 151 (2020), 111972, <https://doi.org/10.1016/j.bios.2019.111972>.
- [25] F.C.B. Fernandes, J.R. Andrade, P.R. Bueno, A nanoscale redox-active composite as a low-fouling interface for capacitive assaying, *Sensor. Actuator. B Chem.* 291 (2019) 493–501, <https://doi.org/10.1016/j.snb.2019.01.164>.
- [26] D. Kang, X. Zuo, R. Yang, F. Xia, K.W. Plaxco, R.J. White, Comparing the properties of electrochemical-based DNA sensors employing different redox tags, *Anal. Chem.* 81 (2009) 9109–9113, <https://doi.org/10.1021/ac901811n>.
- [27] D. Mwanza, S. Phal, T. Nyokong, S. Tesfalidet, P. Mashazi, Electrografting of isophthalic acid monolayer and covalent attachment of antibody onto carbon surfaces: construction of capacitive biosensor for methotrexate detection, *Electrochim. Acta* 398 (2021), 139360, <https://doi.org/10.1016/j.electacta.2021.139360>.
- [28] S. Phal, B. Lindholm-Sethson, P. Geladi, A. Shchukarev, S. Tesfalidet, Determination of Methotrexate in spiked human blood serum using multi-frequency electrochemical impedance spectroscopy and multivariate data analysis, *Anal. Chim. Acta* 987 (2017) 15–24, <https://doi.org/10.1016/j.aca.2017.08.034>.
- [29] S. Phal, B. Shatri, A. Berisha, P. Geladi, B. Lindholm-Sethson, S. Tesfalidet, Covalently electrografted carboxyphenyl layers onto gold surface serving as a platform for the construction of an immunosensor for detection of Methotrexate, *J. Electroanal. Chem.* 812 (2018) 235–243, <https://doi.org/10.1016/j.jelechem.2017.12.072>.
- [30] S. Tesfalidet, P. Geladi, K. Shimizu, B. Lindholm-Sethson, Detection of Methotrexate in a flow system using electrochemical impedance spectroscopy and multivariate data analysis, *Anal. Chim. Acta* 914 (2016) 1–6, <https://doi.org/10.1016/j.aca.2016.02.012>.
- [31] X. Lu, A. Miodok, W.M. Munief, P. Jolly, V. Pachauri, X. Chen, P. Estrela, S. Ingebrandt, Reduced graphene-oxide transducers for biosensing applications beyond the Debye-screening limit, *Biosens. Bioelectron.* 130 (2019) 352–359, <https://doi.org/10.1016/j.bios.2018.09.045>.
- [32] O.K. Adeniyi, P.N. Mashazi, Stable thin films of human P53 antigen on gold surface for the detection of tumour associated anti-P53 autoantibodies, *Electrochim. Acta* 331 (2020), 135272, <https://doi.org/10.1016/j.electacta.2019.135272>.
- [33] W.M. Bullis, Standard Measurements of the Resistivity of Silicon by the Four-Probe Method, 1974.
- [34] O. Adeniyi, N. Nwahara, D. Mwanza, T. Nyokong, P. Mashazi, Nanohybrid electrocatalyst based on cobalt phthalocyanine-carbon nanotube-reduced graphene oxide for ultrasensitive detection of glucose in human saliva, *Sensor. Actuator. B Chem.* 348 (2021), 130723, <https://doi.org/10.1016/j.snb.2021.130723>.
- [35] J.H. Park, J.A. Jackman, A.R. Ferhan, G.J. Ma, B.K. Yoon, N.J. Cho, Temperature-induced denaturation of BSA protein molecules for improved surface passivation coatings, *ACS Appl. Mater. Interfaces* 10 (2018) 32047–32057, <https://doi.org/10.1021/acami.8b13749>.
- [36] J. Sabaté del Río, O.Y.F. Henry, P. Jolly, D.E. Ingber, An antifouling coating that enables affinity-based electrochemical biosensing in complex biological fluids, *Nat. Nanotechnol.* 14 (2019) 1143–1149, <https://doi.org/10.1038/s41565-019-0566-z>.
- [37] D. Mwanza, O. Adeniyi, S. Tesfalidet, T. Nyokong, P. Mashazi, Capacitive label-free ultrasensitive detection of PSA on a covalently attached monoclonal anti-PSA antibody gold surface, *J. Electroanal. Chem.* (2022), 116983, <https://doi.org/10.1016/j.jelechem.2022.116983>.
- [38] X. Hu, J. Tian, C. Li, H. Su, R. Qin, Y. Wang, X. Cao, P. Yang, Amyloid-like protein aggregates: a new class of bioinspired materials merging an interfacial anchor with antifouling, *Adv. Mater.* 32 (2020) 1–11, <https://doi.org/10.1002/adma.202000128>.
- [39] P.K. Sharma, G. Gupta, V.V. Singh, B.K. Tripathi, P. Pandey, M. Boopathi, B. Singh, R. Vijayaraghavan, Synthesis and characterization of polypyrrole by cyclic voltammetry at different scan rate and its use in electrochemical reduction of the simulant of nerve agents, *Synth. Met.* 160 (2010) 2631–2637, <https://doi.org/10.1016/j.synthmet.2010.10.016>.
- [40] F. Fusilba, D. Bélanger, Electropolymerization of polypyrrole and polyaniline-polypyrrole from organic acidic medium, *J. Phys. Chem. B* 103 (1999) 9044–9054, <https://doi.org/10.1021/jp9916790>.
- [41] U. Páramo-García, J.G. Ibanez, N. Batina, Electrochemical modulation of the thickness of polypyrrole films by using different anionic dopants, *Int. J. Electrochem. Sci.* 6 (2011) 5172–5188, [https://doi.org/10.1016/S1452-3981\(23\)18397-0](https://doi.org/10.1016/S1452-3981(23)18397-0).
- [42] A.K. Prusty, S. Bhand, A capacitive immunosensor for tetracycline estimation using antibody modified poly(amine-alkanethiol) ultra-thin film on gold, *J. Electroanal. Chem.* 863 (2020), 114055, <https://doi.org/10.1016/j.jelechem.2020.114055>.
- [43] S. Zheng, M. Bawazir, A. Dhall, H.E. Kim, L. He, J. Heo, G. Hwang, Implication of surface properties, bacterial motility, and hydrodynamic conditions on bacterial surface sensing and their initial adhesion, *Front. Bioeng. Biotechnol.* 9 (2021) 1–22, <https://doi.org/10.3389/fbioe.2021.643722>.

- [44] H.A. Bruck, M. Yang, Y. Kostov, A. Rasooly, Electrical percolation based biosensors, *Methods* 63 (2013) 282–289, <https://doi.org/10.1016/j.ymeth.2013.08.031>.
- [45] J. Bausells, H. Ben Halima, F.G. Bellagambi, A. Alcacer, N. Pfeiffer, M. Hangouët, N. Zine, A. Errachid, On the impedance spectroscopy of field-effect biosensors, *Electrochem. Sci. Adv.* 2 (2022) 1–16, <https://doi.org/10.1002/elsa.202100138>.
- [46] Y. Li, R. Han, M. Chen, X. Yang, Y. Zhan, L. Wang, X. Luo, Electrochemical biosensor with enhanced antifouling capability based on amyloid-like bovine serum albumin and a conducting polymer for ultrasensitive detection of proteins in human serum, *Anal. Chem.* 93 (2021) 14351–14357, <https://doi.org/10.1021/acs.analchem.1c04153>.
- [47] F. Wang, Y. Wu, J. Liu, B. Ye, *Electrochimica Acta* DNA Langmuir – Blodgett Modified Glassy Carbon Electrode as Voltammetric Sensor for Determinate of Methotrexate, vol. 54, 2009, pp. 1408–1413, <https://doi.org/10.1016/j.electacta.2008.09.027>.
- [48] M.T.X. Cal, *ARKTM Methotrexate Assay Application Ortho Clinical Diagnostics VITROS[®] XT 7600 Integrated System*, 2019, pp. 2–7.
- [49] C. Wolfrom, R. Hepp, R. Hartmann, H. Breithaupt, G. Henze, Pharmacokinetic study of methotrexate, folinic acid, and their serum metabolites in children treated with high-dose Methotrexate and leucovorin rescue, *Eur. J. Clin. Pharmacol.* 39 (1990) 377–383, <https://doi.org/10.1007/BF00315414>.